

William S. Oates

Department of Mechanical Engineering,
Florida A&M/Florida State University,
Tallahassee, FL 32310-6046
e-mail: woates@eng.fsu.edu

Phillip G. Evans

Department of Mechanical Engineering,
Ohio State University,
Columbus, OH 43210
e-mail: evans.895@osu.edu

Ralph C. Smith

Center for Research in Scientific Computation,
Department of Mathematics,
North Carolina State University,
Raleigh, NC 27695
e-mail: rsmith@eos.ncsu.edu

Marcelo J. Dapino

Department of Mechanical Engineering,
Ohio State University,
Columbus, OH 43210
e-mail: dapino.1@osu.edu

Experimental Implementation of a Hybrid Nonlinear Control Design for Magnetostrictive Actuators

A hybrid nonlinear optimal control design is experimentally implemented on a magnetostrictive Terfenol-D actuator to illustrate enhanced tracking control at relatively high speed. The control design employs a homogenized energy model to quantify rate-dependent nonlinear and hysteretic ferromagnetic switching behavior. The homogenized energy model is incorporated into a finite-dimensional nonlinear optimal control design to directly compensate for the nonlinear and hysteretic magnetostrictive constitutive behavior of the Terfenol-D actuator. Additionally, robustness to operating uncertainties is addressed by incorporating proportional-integral (PI) perturbation feedback around the optimal open loop response. Experimental results illustrate significant improvements in tracking control in comparison to PI control. Accurate displacement tracking is achieved for sinusoidal reference displacements at frequencies up to 1 kHz using the hybrid nonlinear control design, whereas tracking errors become significant for the PI controller for frequencies equal to or greater than 500 Hz. [DOI: 10.1115/1.3089560]

Keywords: nonlinear optimal tracking, magnetostrictive, rate dependence, perturbation control

1 Introduction

The role of smart materials continues to be a critical part of technology development in many biomedical, automotive, aerospace, and industrial applications. These materials provide advantages in applications where large forces and small displacements are desired over a broad frequency range with high precision. The solid state characteristics of these materials provide compact actuators, which are critical in applications where size and weight are important. A large number of these applications employ piezoelectric or magnetostrictive materials, which respectively possess electric or magnetic field induced displacement and force. For example, single crystal ferroelectric relaxors (lead magnesium niobate-lead titanate (PMN-PT) or lead zirconate-lead titanate (PZN-PT)) have provided significant advances in sonar transducer applications due to their efficiency and relatively high strain behavior ($\leq 1\%$) [1]. Additionally ferroelectric lead zirconate titanate (PZT) has been successfully implemented in commercial nanopositioning stages for controlling the position of material specimens for probing atomic structures using atomic force microscopy and scanning probe microscopy [2]. The robustness of magnetostrictive terbium-iron-dysprosium (Terfenol-D) actuators has provided reliable actuator designs for several applications, including precisely machined out-of-round piston heads by effectively controlling the cutting tool position [3].

Although ferroic materials have been successfully implemented in a number of applications, limitations associated with nonlinear and hysteretic material behavior have presented challenges in developing high performance actuation response over a broad frequency range. The nonlinear and hysteretic material behavior is primarily due to the reorientation of local electric or magnetic variants that align with the applied electric or magnetic fields. Moderate to large field levels can induce 0.1% strain in polycrystalline PZT [4] and up to 6% strain in single crystal ferromagnetic shape memory alloys [5]; at these field levels, obtaining accurate

and precise control is greatly complicated by nonlinearities and magnetic hysteresis. Moreover, small excitations near resonance may also introduce non-negligible hysteresis with deformation comparable to large excitations away from resonance (excluding dc). These issues have motivated research in developing new control designs that can effectively compensate for nonlinearities and hysteresis induced by ferroelectric or ferromagnetic switching while still providing accurate forces or displacements over a broad frequency range.

Two general strategies are typically considered when developing a control design to compensate for nonlinearities and hysteresis. These two strategies illustrated in Fig. 1 are characterized by either a nonlinear inverse compensator or direct nonlinear control. The approach illustrated in Fig. 1(a) employs a nonlinear inverse compensator, which approximately linearizes the constitutive behavior so that linear control methods can be employed [6–11]. This approach provides the ability to implement well-developed linear control laws. It can also be advantageous in applications where an unknown disturbance load is present or the reference signal is not known well in advance; however, this advantage is only realized if the constitutive model is efficient enough to be inverted in real time. The second strategy illustrated in Fig. 1(b) entails direct incorporation of the material model into the control design so that the nonlinear control input is directly determined. This circumvents issues associated with computing the constitutive inverse law but introduces challenges in identifying robust numerical algorithms that can achieve convergence efficiently. The second strategy is implemented here where a nonlinear open loop control signal is computed off-line, and perturbation feedback is then introduced to improve robustness when operating uncertainties are present.

Both of the inverse compensator and nonlinear control designs require an efficient and accurate constitutive model that can quantify the nonlinear and hysteretic ferroic switching behavior. A significant amount of literature is available describing various approaches for modeling ferromagnetic and magnetostrictive materials (e.g., see Refs. [12–16]). For control applications, Preisach models are often considered for quantifying nonlinear and hysteretic material behavior in ferromagnetic materials due to

Contributed by the Dynamic Systems, Measurement, and Control Division of ASME for publication in the JOURNAL OF DYNAMIC SYSTEMS, MEASUREMENT, AND CONTROL. Manuscript received August 30, 2007; final manuscript received December 8, 2008; published online April 29, 2009. Assoc. Editor: Nader Jalili.

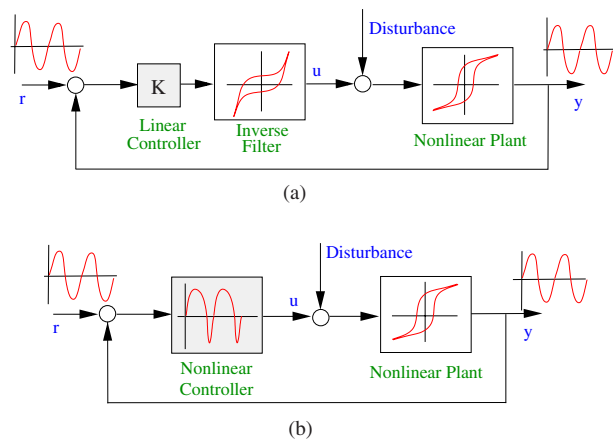


Fig. 1 Examples of nonlinear control designs. (a) Nonlinear inverse compensator. (b) Direct nonlinear control.

their computational efficiency for real-time applications (e.g., see Refs. [8,17]). These models have the disadvantage of requiring a large number of nonphysical parameters to accurately predict minor loop hysteresis. In the analysis presented here, a ferroic homogenized energy model is implemented, which utilizes fundamental energy relations at the mesoscopic or lattice length scale to quantify macroscopic constitutive behavior in ferroic materials. The model utilizes a multiscale approach that relates local material inhomogeneities using a stochastic framework to quantify macroscopic material behavior [18–27]. This modeling framework has been successful in modeling rate-dependent major and minor hysteresis loops in several ferroelectric, magnetostrictive, and shape memory alloy compositions (see Ref. [22] for a review). The stochastic modeling approach utilizes general densities, which can be fitted to experimental results. This improves model prediction, which is critical in model-based control designs so that the amount of feedback required to achieve a specified performance criteria is reduced.

The second strategy in developing a model-based nonlinear control design is presented here where the constitutive law is directly incorporated into an optimal control design. This approach is shown to improve tracking control accuracy for a magnetostrictive transducer at frequencies up to 1 kHz. The authors are only aware of one other model-based control design successfully implemented experimentally on a similar magnetostrictive actuator [8]. In their analysis, a Preisach-based nonlinear inverse compensator was employed. The reference displacement was limited to aperiodic signals centered around 30 Hz, and tracking control was improved in comparison to proportional control. In the analysis presented here, comparisons between the nonlinear optimal control design and classical proportional-integral (PI) control are conducted. It is demonstrated that PI tracking control performance begins to degrade for sinusoidal reference displacements with frequencies at or above 500 Hz. The bandwidth of the actuator is improved by directly incorporating the constitutive behavior within the control design. Reasonable tracking control is achieved for frequencies up to at least 1 kHz.

The experimental analysis presented here utilizes a nonlinear control design previously analyzed numerically for controlling a magnetostrictive transducer operating in the current control mode [24,25]. The model is extended to include voltage control to accommodate the experimental setup and is validated over a broader range of frequencies (100–1000 Hz) than previous numerical analyses. In Sec. 2, the experimental setup is described. In Sec. 3, the constitutive model and the dynamic model are presented and compared with open loop actuator characterizations. In Sec. 4, the nonlinear control design is presented and compared with classic PI control to identify operating regimes where the nonlinear con-

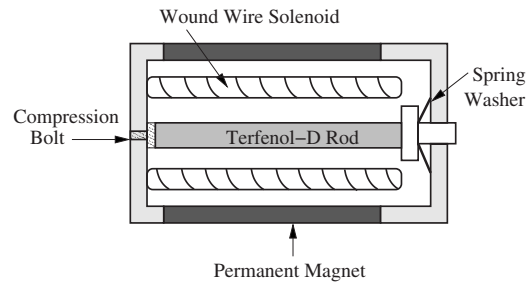


Fig. 2 Schematic of the Terfenol-D actuator used in the control experiments

trol design provides enhanced performance. Section 5 presents the tracking control experimental results. Section 6 includes discussion and concluding remarks.

2 Experimental Implementation

The validation of the proposed control method was performed on an Etrema Products, Inc. (Ames, IA), magnetostrictive Terfenol-D actuator model MFR OTY77. The actuator employs a Terfenol-D rod 12.5 mm in diameter by 100 mm in length, which is subjected to a 10–14 MPa preload and an ~ 40 kA/m magnetic field bias from a permanent magnet. The drive coil rating is 6.2 kA/m A with a 3.4 A_{rms} limit. Figure 2 illustrates the basic internal components in the Etrema actuator, which includes a Terfenol-D rod, a compression bolt and a spring washer to preload the rod, a surrounding wound wire solenoid, and a permanent magnet.

The drive voltage is generated by a 16 bit digital-to-analog converter (DAC) on a dSPACE DS1104 controller board, which has an output range of 10 V and >80 dB signal-to-noise ratio. The drive voltage is amplified by an AE Techron LVC 5050 linear amplifier set to a gain of 17 V/V. The bandwidth of the amplifier is 20 kHz.

Reported data include the DS1104 drive voltage, actuator current, and actuator strain. The current supplied to the actuator is measured by the Techron's current monitor, which outputs 1 V for every 3 A of current. The current monitor signal is sampled using the 16 bit analog-to-digital (ADC) on the DS1104 board. The strain measurement is simultaneously sampled with the same ADC from a Lion Precision capacitive sensor (PX405JTC probe with DMT10R driver) with a sensitivity of 0.257 mm/V and a bandwidth of 12.5 kHz. An Omega Engineering, Inc. (Stamford, CT) signal amplifier model OMNI-AMP III dc with a gain of 10 V/V and a bandwidth of 10 kHz is used to match the dynamic range of the strain measurement with the range of the ADC.

Tests were set up as block diagrams using Mathworks (Natick, MA) SIMULINK. The block diagrams were then compiled and downloaded to the DS1104 controller using REAL TIME WORKSHOP, also by Mathworks. Data were acquired using CONTROLDESK by dSPACE with a sample frequency of 10 kHz.

3 Model Development

The modeling framework used in implementing the control design incorporates magnetostrictive nonlinearities and hysteresis into an actuator model. The ferromagnetic switching behavior is modeled using a homogenized energy model that is based on previous work described in detail in Refs. [18–23]. Here, only key equations are given to motivate the implementation of the constitutive model in the structural dynamic model and control design. The homogenized energy model is formulated using an applied magnetic field; however, the power amplifier used in the control experiments uses voltage control. Although a hardware modification can be employed to run the power amplifier in current control, the homogenized energy model was extended to relate voltage to current to simplify experimental implementation. This

approach results in directly determining the nonlinear voltage control input from the homogenized energy model, structural dynamic relations, and optimal control design.

In addition to quantifying the ferromagnetic switching behavior, the structural dynamics of the actuator are quantified using a lumped parameter model. Although a distributed weak partial differential equation (PDE) formulation can be employed to incorporate spatial dependence along the actuator length, the operating frequencies considered are below resonance; therefore, a lumped parameter model reasonably approximates the structural dynamics for the sinusoidal reference displacement signals used in validating the control design. For more general reference displacements, such as a step input that excites higher order harmonics, a finite element model may be necessary. Finite element models can be directly incorporated into the model and control design, as discussed in Refs. [22,24,25].

First the homogenized energy model is briefly summarized. Second, the equations associated with the structural dynamic model are summarized to quantify displacements predicted by the homogenized energy model for a magnetic field input. The nonlinear electrical impedance of the amplifier-actuator system is then modeled to relate the magnetic field to the voltage input for controlling the Terfenol-D actuator using voltage control. Lastly, the homogenized energy model is compared with experimental results.

3.1 Rate-Dependent Ferromagnetic Homogenized Energy Model. We summarize here the ferromagnetic homogenized energy model and illustrate how it is used to develop a constitutive model. The model is employed in Sec. 3.2 to construct a structural model for a Terfenol-D actuator, which is later used in the control design. Details regarding the constitutive model formulation can be found in Refs. [19,22,23].

For the Terfenol-D transducer depicted in Fig. 2, we focus on a 1D model in accordance with the uniaxial loading and applied fields. The model is constructed in two steps: (i) development of mesoscopic magnetization relations based on energy principles and (ii) use of stochastic homogenization techniques to construct macroscopic constitutive relations.

We first consider the construction of lattice-level Gibbs energy relations,

$$G(H, \sigma, M, \varepsilon) = \psi(M) + \frac{1}{2} Y^M \varepsilon^2 - a_1 (M - M^r) \varepsilon - a_2 (M - M^r)^2 \varepsilon - \mu_0 H M - \sigma \varepsilon \quad (1)$$

for uniform, homogeneous, isothermal, single crystal materials. Here H , M , ε , and σ , respectively, denote the applied magnetic field, magnetization, strain, and uniaxial applied stress. Furthermore, ψ , Y^M , a_1 , a_2 , μ_0 , and M^r denote a magnetic Helmholtz energy, Young's modulus, piezomagnetic coupling coefficient, magnetostrictive coupling coefficient, free space permeability, and a bias magnetization (e.g., positive remanence). We note that in the Gibbs relation (1), H, σ constitute independent variables, whereas M, ε are dependent variables.

As detailed in Ref. [23], the Ising principles can be used to construct a temperature-dependent magnetic Helmholtz energy relation that incorporates the ferromagnetic to paramagnetic phase transition and provides noncongruent hysteresis kernels. Although based on statistical mechanics tenets, the resulting models are computationally intensive to implement and hence are better suited for material analysis and characterization than real-time control implementation.

Alternatively, one can employ Taylor expansions about equilibria in the Helmholtz energy relation derived from statistical mechanics principles to obtain piecewise quadratic magnetic Helmholtz relations of the form

$$\psi(M) = \begin{cases} \frac{1}{2} \eta (M + M_I)^2, & M \leq -M_I \\ \frac{1}{2} \eta (M - M_I)^2, & M \geq M_I \\ \frac{1}{2} \eta (M_I - M^r) \left(\frac{M^2}{M_I} - M^r \right), & |M| < M_I \end{cases} \quad (2)$$

where η denotes the reciprocal slope dH/dM after switching and M_I is the positive inflection point. We focus primarily on this Helmholtz relation in subsequent model development due to its implementation efficiency.

For operating regimes in which thermal after-effects are negligible, the local magnetization \bar{M} is determined from the conditions

$$\frac{\partial G}{\partial M} = 0, \quad \frac{\partial^2 G}{\partial M^2} > 0 \quad (3)$$

As detailed in Ref. [23], use of the statistical mechanics Helmholtz relation yields Ising kernels of the form

$$\bar{M}(H) = M_s \tanh\left(\frac{H + \alpha M}{a(T)}\right) \quad (4)$$

when magnetoelastic effects are neglected. In agreement with experimental data (and in contrast to classical Preisach models), these kernels are noncongruent and illustrate the role of interaction fields $H_I = \alpha M$ in the effective field $H_e = H + H_I$. Alternatively, use of the Helmholtz relation (2) yields piecewise linear kernels that accommodate reversible postswitching behavior (see Refs. [22,23] for details).

To incorporate the thermal relaxation mechanisms that produce phenomena such as after-effects, one can balance the Gibbs energy G with the relative thermal energy kT/V via the Boltzmann relation

$$\mu(G) = C e^{-GV/kT} \quad (5)$$

where V is a representative volume element at the mesoscopic length scale, k is Boltzmann's constant, and the constant C is specified to ensure integration to unity. We note that Eq. (5) quantifies the probability of achieving an energy level $G(H, \sigma, M, \varepsilon)$ for a given applied stress σ or magnetic field H .

As detailed in Refs. [19,22,23], this yields mesoscopic magnetization relations

$$\bar{M} = x_+ \langle M_+ \rangle + x_- \langle M_- \rangle \quad (6)$$

where x_+ and x_- denote the fraction of moments having positive and negative orientations; hence $x_+ + x_- = 1$ and

$$\langle M_+ \rangle = \int_{M_I}^{\infty} M \mu(G) dM, \quad \langle M_- \rangle = \int_{-\infty}^{-M_I} M \mu(G) dM \quad (7)$$

denote the magnetizations associated with positively and negatively oriented moments—note that ∞ and $-\infty$ can be replaced by the saturation magnetizations M_s and $-M_s$ for the statistical mechanics Helmholtz kernel relation.

The local relations (4) and (6) or the piecewise linear relation resulting from Eq. (3) yields macroscopic magnetization models for homogeneous materials with uniform effective fields. To obtain macroscopic models for polycrystalline, nonhomogeneous materials with distributed effective fields, as motivated by Eq. (4), we make the assumption that the coercive fields H_c and interaction fields H_I are manifestations of underlying densities $\nu_c(H_c)$ and $\nu_I(H_I)$ rather than constants. For the operating regimes under consideration, it has been observed that preload levels are sufficiently large so as to render dynamic stress effects on the magnetization as negligible. Hence we neglect effects due to stress and strain contributions to the Gibbs energy and employ the macroscopic model

Table 1 Parameters employed in the homogenized energy model where χ_m denotes the magnetic susceptibility, $\gamma = V/kT$ is the reciprocal of the relative thermal energy, M' is the local remanent magnetization, and τ is the time constant (see Ref. [22] for details)

$\chi_m = 3.3$
$\gamma = 1.23 \times 10^8 \text{ ms}^2/\text{kg}$
$M' = 190 \text{ kA/m}$
$\tau = 1.15 \times 10^{-4} \text{ s}$

$$[M(H)](t) = \int_{-\infty}^{\infty} \int_0^{\infty} \nu(H_c, H_I) [\bar{M}(H + H_I; H_c, \xi)](t) dH_I dH_c \quad (8)$$

where $\nu(H_c, H_I) = \nu_c(H_c) \nu_I(H_I)$ and ξ denotes the initial distribution of moments. Examples illustrating the model performance for regimes that exhibit after-effects, including creep behavior and nonclosure of biased minor loops, can be found in Refs. [23,26]. Details regarding the extension of the framework to incorporate magnetomechanical coupling are provided in Ref. [27].

We note that for certain operating regimes, a priori choices of normal and lognormal relations for $\nu_I(H_I)$ and $\nu_c(H_c)$ provide sufficient accuracy. For general operating regimes requiring high accuracy, the techniques detailed in Refs. [21,22] for general density identification can be employed.

Whereas the homogenized energy model can be interpreted as providing an energy basis for certain extended Preisach models, it differs from the classical Preisach model (characterized by the properties of deletion and congruency) in five fundamental aspects. (i) The energy basis permits correlation of certain parameters with measured properties of the data. (ii) The energy basis permits the direct incorporation of temperature or stress dependencies in the kernel or basis rather than the parameters or weights. (iii) Derivation of the theory from Boltzmann principles yields models that directly incorporate the after-effects and minor loop nonclosure measured for certain materials and operating regimes. (iv) Derivation of the model using Helmholtz relations derived from statistical mechanics principles yields kernels or hysterons that incorporate the noncongruency measured for certain operating regimes and materials. (v) The framework automatically incorporates reversible magnetization mechanisms for small ac field excursions about a fixed dc value. Additional discussion detailing similarities and differences between this framework and Preisach models can be found in Refs. [22,23].

For operating regimes in which internal damping is considered negligible, the condition $\frac{\partial G}{\partial \epsilon} = 0$, for G given by Eq. (1) yields the magnetoelastic constitutive relation

$$\sigma = Y^M \epsilon - a_1(M(H) - M') - a_2(M(H) - M')^2$$

To incorporate internal damping, one can posit that stress is proportional to a linear combination of strain ϵ and strain rate $\dot{\epsilon}$, in the absence of applied fields, to obtain the constitutive relation

$$\sigma = Y^M \epsilon + c_D \dot{\epsilon} - a_1(M(H) - M') - a_2(M(H) - M')^2 \quad (9)$$

where c_D denotes the Kelvin–Voigt damping coefficient. We employ this relation, with M given by Eq. (8), in subsequent model development.

The material parameters for the homogenized energy model are given in Table 1. These parameters were identified from the experimental results presented in Sec. 3.4 using parameter optimization techniques detailed in Ref. [22]. The parameter optimization utilizes a MATLAB constrained optimization algorithm coupled to the homogenized energy model to quantify a set of parameters based on a quadratic cost between the model displacement and the measured displacement. Note that these parameters are not unique since magnetic induction was not measured. Furthermore, many

Table 2 Model parameters for the magnetostrictive actuator and damped oscillator. The parameter optimization identified the magnetostrictive coefficient a_2 to be zero for the considered operating regime.

$\bar{k} = 1.96 \times 10^7 \text{ N/m}$
$a_1 = 3275 \text{ N/A m}$
$a_2 = 0 \text{ N m}^2/\text{A}^2$
$\bar{m} = 0.013 \text{ kg}$
$\bar{c}_D = 2.3 \times 10^3 \text{ N s/m}$
$A = 1.27 \times 10^{-4} \text{ m}^2$

of the material parameters are often dependent on the field magnitude and internal magnetization state. Here, variations in the magnetostrictive, piezomagnetic, and permeability are included in the model via the ferromagnetic switching and homogenization approach. Conversely, variations in the elastic modulus is neglected. The model fits are based on average elastic properties at the bias field, as illustrated in Fig. 4.

The parameter optimization was conducted using experimental displacement measurements and was compared with the current applied to the solenoid in the magnetostrictive actuator. This identification procedure requires implementing the structural model described in the following section. Moreover, the structural parameters given in Table 2 were also determined using parameter optimization to obtain a complete set of material parameters for use in the control design.

3.2 Structural Model. The constitutive relations given by Eqs. (8) and (9) are used to develop a system model that quantifies forces and displacements when a magnetic field or stress is applied to the magnetostrictive actuator. The PDE model is first given and is then reformulated as a lumped parameter ordinary differential equation (ODE). The effective stiffness, mass, and damping factor are determined from the parameter optimization, which is based on the structural dynamics of the Terfenol-D actuator and the damped oscillator used in preloading the actuator. A simple schematic of this configuration is illustrated in Fig. 3.

A balance of forces gives

$$\rho A \frac{\partial^2 w}{\partial t^2} = \frac{\partial N_{\text{tot}}}{\partial x} \quad (10)$$

where the density of the actuator is denoted by ρ , the cross-section area is A , and the displacement is denoted by w (see Refs. [22,28] for details). The total force N_{tot} acting on the actuator is

$$N_{\text{tot}}(t, x) = -Y^M A \frac{\partial w}{\partial x} - c_D A \frac{\partial^2 w}{\partial x \partial t} + A[a_1(M(H) - M') + a_2(M(H) - M')^2] \quad (11)$$

where the hysteretic and nonlinear H - M relation is quantified by Eq. (8). The model quantifies relative displacements from the preloaded reference state. The linear elastic strain component in the

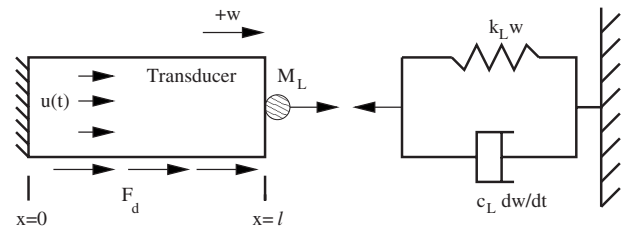


Fig. 3 Magnetostrictive actuator with a damped oscillator used to quantify loads under a time varying magnetic field. Disturbance forces along the actuator are given by F_d , and the control input is $u(t)$.

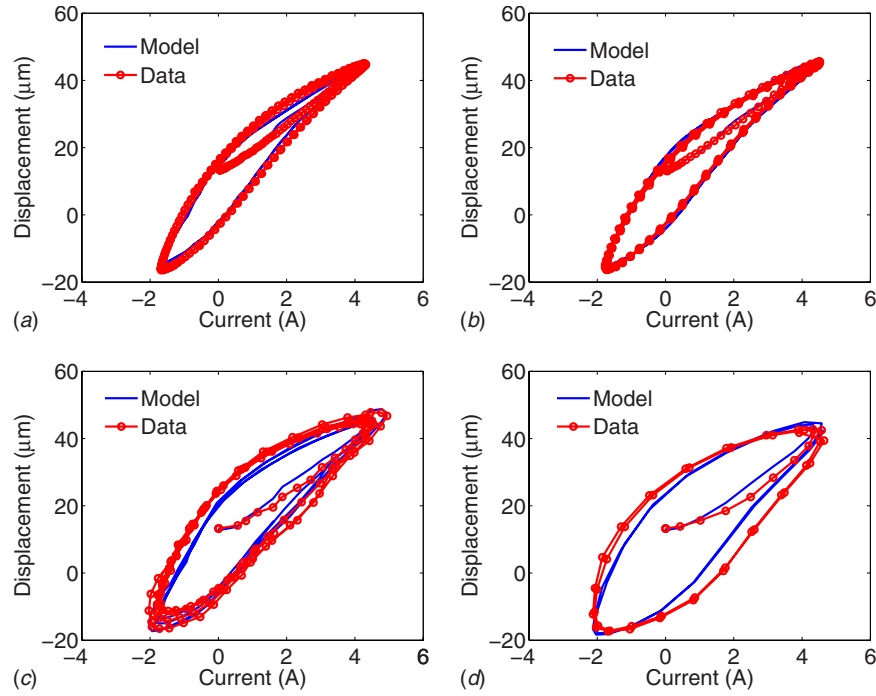


Fig. 4 Rate-dependent constitutive data and comparison to the homogenized energy model described in Sec. 3. The frequencies tested and fitted to the model were (a) 100 Hz, (b) 200 Hz, (c) 300 Hz, and (d) 500 Hz.

direction of loading is defined by $\varepsilon = \partial w / \partial x$. Differentiation of the spatially invariant magnetization relation in Eq. (11) is equivalent to differentiating a characteristic or Heaviside function over the interval $[0, \ell]$ spanned by the rod. This yields a Dirac distribution at the end of the rod, which diminishes the convergence properties of standard approximation techniques. This is avoided through the use of conventional weak formulations, as detailed in Ref. [22].

The mechanical, piezomagnetic, and magnetostrictive parameters obtained through parameter optimization are given in Table 2. These parameters, in addition to parameters given in Table 1, were obtained for operating regimes used in the control design. This operating regime was restricted to minor hysteresis loops around a magnetization state that is affected by the permanent magnetization bias (see Fig. 2) and a biased magnetic field required to track the reference signal later described in Sec. 4. These plots are shown later in Fig. 4. For this operating regime, the magnetostrictive coefficient was determined to be zero. The combination of biased field and magnetization results in model fits in operating regimes where the material behavior can be sufficiently described by piezomagnetic coupling. For example, if the magnetostrictive coupling is approximated by taking the first term in a Taylor series expansion around a biased magnetization M_0 of the Terfenol-D rod actuator, the effective piezomagnetic coefficient is

$$\bar{a}_1 = a_1 + 2a_2 M_0 \quad (12)$$

In general, this would not be true if the model was fit to the full hysteresis loop.

As illustrated in Fig. 3, the boundary conditions are defined by a zero displacement at $x=0$, and the balance of forces at $x=\ell$ yields

$$N_{\text{tot}}(t, \ell) = -k_L w(t, \ell) - c_L \frac{\partial w}{\partial t}(t, \ell) - m_L \frac{\partial^2 w}{\partial t^2}(t, \ell) \quad (13)$$

The initial conditions are $w(0, x) = 0$ and $\partial w / \partial x(0, x) = 0$.

3.2.1 Lumped Parameter Model. The distributed parameter system described in the previous section is approximated as a lumped parameter model for implementation within the control

design. Here, the tracking problem is focused on sinusoidal reference signals that are well below the resonance of the Terfenol-D actuator. When more general reference signals or significant disturbances are considered, the distributed parameter model should be discretized using methods such as finite elements (see Ref. [29] for an example of controlling vibration of thin plates).

In the lumped parameter case, the second order differential equation given by Eq. (10) with boundary conditions (13) is rewritten in the form

$$\bar{m}\ddot{y} + \bar{c}_D\dot{y} + \bar{k}y = F_m(H) + F_d \quad (14)$$

where \bar{m} , \bar{c}_D , and \bar{k} denote the effective mass, damping, and stiffness coefficients, respectively. The displacement at the end of the rod is denoted by $y(t)$. These parameters represent the effective structural dynamic coefficients for the Terfenol-D rod and damped oscillator, which are determined using the parameter optimization as described in Sec. 3.2. These model parameters associated with the magnetostrictive actuator and damped oscillator are given in Table 2.

For control implementation, Eq. (14) can be reformulated as a first order system,

$$\dot{\mathbf{x}}(t) = \mathbf{A}\mathbf{x}(t) + [\mathbf{B}(u)](t) + \mathbf{G}(t)$$

$$\mathbf{x}(0) = \mathbf{x}_0$$

$$y(t) = \mathbf{C}\mathbf{x}(t) \quad (15)$$

where $\mathbf{x}(t) = [y, \dot{y}]^T$. The matrix \mathbf{A} incorporates the mass, damping, and stiffness matrices given in Eq. (14), and $[\mathbf{B}(u)](t)$ includes the nonlinear input where $u(t)$ is defined as the magnetic field. The disturbances are denoted by the matrix $\mathbf{G}(t)$. These matrices are given below in Eq. (16). The initial conditions are defined by \mathbf{x}_0 . The output of the system $y(t)$ is a function of the system states according to the matrix $\mathbf{C} = [1, 0]$, where only the displacement at the end of the actuator is measurable,

$$\mathbf{A} = \begin{bmatrix} 0 & 1 \\ -\bar{k}/\bar{m} & -\bar{c}_D/\bar{m} \end{bmatrix}, \quad \mathbf{B}(u) = F_m(u) \begin{bmatrix} 0 \\ 1/\bar{m} \end{bmatrix}, \quad (16)$$

$$\mathbf{G}(t) = F_d(t) \begin{bmatrix} 0 \\ 1/\bar{m} \end{bmatrix}$$

The constitutive modeling results at multiple frequencies using Eq. (15) are illustrated in Fig. 4 and compared with experimental results. A reasonable estimation of rate-dependent hysteresis is achieved over the frequency range of 100–500 Hz using the parameters in Tables 1 and 2. However, voltage control is used in the control experiments; therefore the model is extended to include nonlinear electrical impedance relations to obtain a model that can quantify the nonlinear voltage control input for experimental implementation.

3.3 Nonlinear Current-Voltage Relations. A lumped circuit model is used to relate the input voltage to the magnetic field applied to the Terfenol-D actuator. The electromagnetics analysis assumes no leakage losses and ideal flux linkage. A linear power amplifier is used in the experiments. The nonlinear impedance associated with the electrical part of the system is assumed to be related to the ferromagnetic switching in the Terfenol-D actuator. This can be modeled using a resistor in series with a nonlinear inductor (i.e., the Terfenol-D rod) and a voltage source that has been amplified by the linear power amplifier.

The nonlinear inductance is quantified by coupling the homogenized energy model with the lumped-electric circuit model. The first order nonlinear ODE for a resistor in series with a nonlinear inductor is

$$L(M) \frac{di(t)}{dt} + Ri(t) = V(t) \quad (17)$$

$$i(0) = i_0$$

where $L(M)$ is the inductance written as a function of magnetization, i is the current, V is the voltage input, R is the resistance, and the initial conditions are defined by i_0 .

The magnetic field H applied to the Terfenol-D rod is related to the current by the relation

$$H = \frac{N}{\ell} i \quad (18)$$

where ℓ is the actuator length and N is the number of coils in the solenoid. Here, the tangential magnetic field on the surface of the Terfenol-D rod is assumed to fully penetrate the rod cross-section area over the frequency range considered. This assumes that the effects of eddy current losses are negligible. Model uncertainties associated with this assumption are discussed in Sec. 6.

The inductance can be related to the magnetic permeability and the wound wire solenoid. From classic electromagnetics [30], the inductance describes the self-induced emf, which is proportional to the time rate of change in current. The inductance can therefore be written as

$$L(M) = \frac{N^2}{\ell} \frac{d\Phi_m(M)}{dH} \quad (19)$$

where N is the number of turns in the solenoid and Φ_m is the flux. The flux is related to the induction through the relation

$$\Phi_m = \int_A \mathbf{B} \cdot d\mathbf{A} \quad (20)$$

where \mathbf{B} is the induction and \mathbf{A} is the surface. Since eddy currents in the Terfenol-D actuator have been neglected and if rod end effects are neglected, the flux can be defined by

$$\Phi_m = BA \quad (21)$$

for the induction component B parallel to the rod length, and A is the cross-sectional area.

The nonlinear inductance can be determined by including changes in the remanent magnetization with respect to the change in field given in Eq. (19). This can be described by representing the magnetization as a superposition of a linear term and the rate-dependent nonlinear and hysteretic term associated with the change in remanent magnetization. This is considered at the macroscopic length scale by writing Eq. (8) as

$$[M(H)](t) = \chi_m H(t) + [M'(H)](t) \quad (22)$$

where $\chi_m = \mu_0(1 + \chi_m)$ is the macroscopic magnetic susceptibility and $M'(H)$ is the remanent magnetization. The induction relation $B = \mu_0(H + M)$ can then be written as

$$[B(H)](t) = \mu_0(1 + \chi_m)H(t) + \mu_0[M'(H)](t) \quad (23)$$

where $\mu_0 = 4\pi \times 10^{-7}$ Wb/A m is the permeability of free space.

The nonlinear induction is then

$$L(M) = \frac{N^2 A}{\ell} \frac{dB}{dH} = \frac{N^2 A}{\ell} \left(\mu_m + \mu_o \frac{dM'}{dH} \right) \quad (24)$$

where μ_m is the relative permeability of the material. Note that this relation simplifies to the classic linear inductance relation for a wound wire solenoid when the remanent magnetization is constant. Whereas this approach is expected to provide a relation for nonlinear inductance, H - B data are not available from the Terfenol-D actuator which requires estimating the inductance. A fitting parameter is introduced according to

$$L(M) = N \frac{dB}{di} \simeq K_L \frac{dy}{di} \quad (25)$$

where y is the Terfenol-D actuator displacement determined from Eq. (15) and K_L is quantified from the experimental results using voltage versus current data and current versus strain data. K_L was quantified at 100 Hz and held fixed for all other frequencies considered in the model-based control design. The value that was quantified from the experiments was $K_L = 2 \times 10^5$ V s/m, which was used in the model and compared with experiment results presented in Sec. 3.4. The nonlinear model is also compared with a linearized lumped circuit model where the remanent magnetization is assumed constant. When the inductance is linearized, the model prediction is reasonable in regimes of positive current for the given frequency range. When the current is negative, more ferromagnetic switching occurs since the Terfenol-D rod was magnetized in the positive direction. This requires implementing the nonlinear inductance model to improve accuracy; therefore, the nonlinear model is used in determining the nonlinear voltage control input.

3.4 Actuator Characterization. Characterization of the actuator was performed using open loop sinusoidal drive voltages at 100 Hz, 200 Hz, 300 Hz, and 500 Hz. Each data set was initiated by a half-cycle of a 1 Hz sine wave with an amplitude of 1 V to the amplifier-actuator system; this corresponds to a current of 4.6 A. After the initial magnetization half-cycle, sinusoidal voltage signals at frequencies of 100 Hz, 200 Hz, 300 Hz, and 500 Hz were used to drive the Terfenol-D actuator. The peak-to-peak sinusoidal voltage inputs were adjusted to achieve minor loops extending 60 μ m. Strain-current minor loops are illustrated in Fig. 4 for the frequencies of 100 Hz, 200 Hz, 300 Hz, and 500 Hz. The corresponding current-voltage loops are illustrated in Fig. 5. The data given in these figures are compared with the homogenized energy model and lumped electric circuit model discussed in the previous sections.

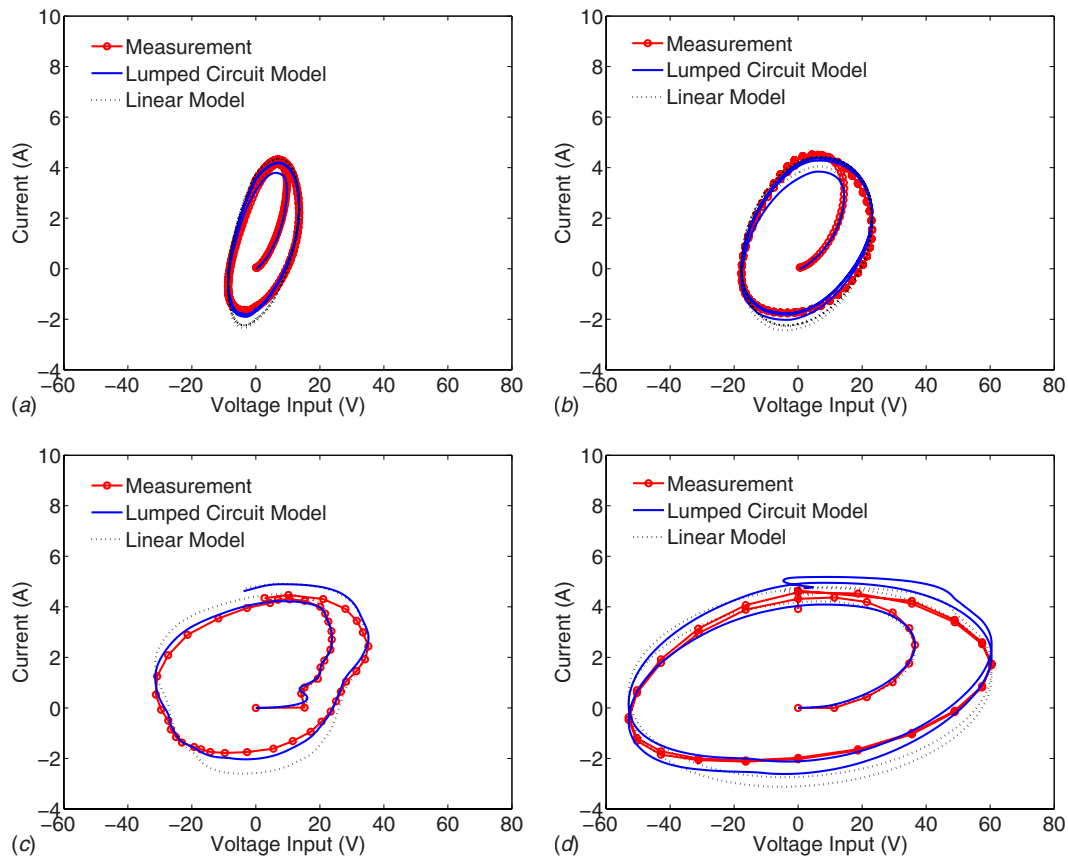


Fig. 5 Current-voltage behavior of the amplifier-actuator system. The data are compared with a linear and nonlinear inductor-resistor lumped circuit model discussed in Sec. 3.3. The frequencies correspond to the data in Fig. 4 where (a) 100 Hz, (b) 200 Hz, (c) 300 Hz, and (d) 500 Hz.

4 Control Design

To provide a metric of comparison for the hybrid nonlinear control design, we compare its tracking performance to a PI control design. First the control gains selected for the PI controller are discussed, and experimental results describing the closed loop dynamics of the PI controller are presented. Second, the fundamental equations describing the nonlinear control design and PI perturbation feedback are given. This follows previous theoretical and numerical analyses of the hybrid nonlinear control design for ferromagnetic actuators; details regarding the algorithm formulation can be found in Refs. [24,25,31]. Previous numerical analysis focused on quantifying a magnetic field control signal and did not consider the electrical impedance of the amplifier-actuator system. The inclusion of the voltage-current dynamics presented in Sec. 3.3 is discussed in this section to illustrate how the open loop nonlinear voltage control signal is implemented experimentally.

4.1 Proportional-Integral Control Design. To facilitate the design of the PI controller, the transfer function of the open loop amplifier-actuator system in the near linear regime was measured using a swept sine voltage input from the DS1104 controller board where the output was the rod tip displacement (see Fig. 6).

The PI controller was designed using the form

$$D(s) = K_P \frac{s + K_I/K_P}{s} \quad (26)$$

where K_P is the proportional gain and K_I is the integral gain. The gain K_P was chosen to move the mechanical resonance peak observed at 4 kHz below 0 dB. The ratio K_P/K_I was chosen so that the phase lag occurred well below the open loop cross-over frequency. Gains of $K_P = 2 \times 10^{-2}$ V/ppm (parts per million) and

$K_P/K_I = 30$ s were chosen. The PI controller boosts the low frequency gain to reduce the steady-state error at the expense of the low frequency phase, as illustrated in Fig. 7(a). The open loop controller-amplifier-actuator transfer function was measured using a swept sine controller input to determine the stability margins (see Fig. 7(b)). The phase margin is 45 deg, and the gain margin is 2. The resulting closed loop bandwidth for PI control is 1140 Hz (see Fig. 8).

4.2 Nonlinear Optimal Tracking Control Design. We summarize here the formulation of a finite-dimensional nonlinear op-

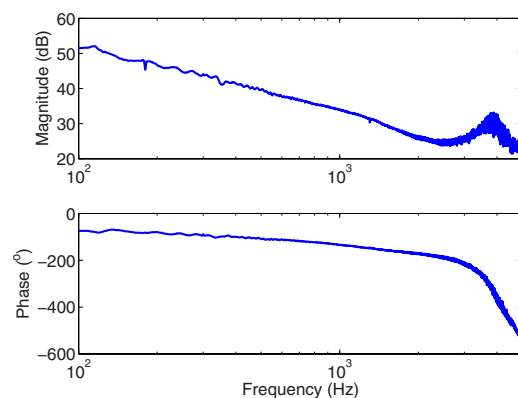


Fig. 6 Open loop frequency response for the Terfenol-D actuator in the operating regime. The input is voltage to the wound wire solenoid, and the output is the rod tip displacement.

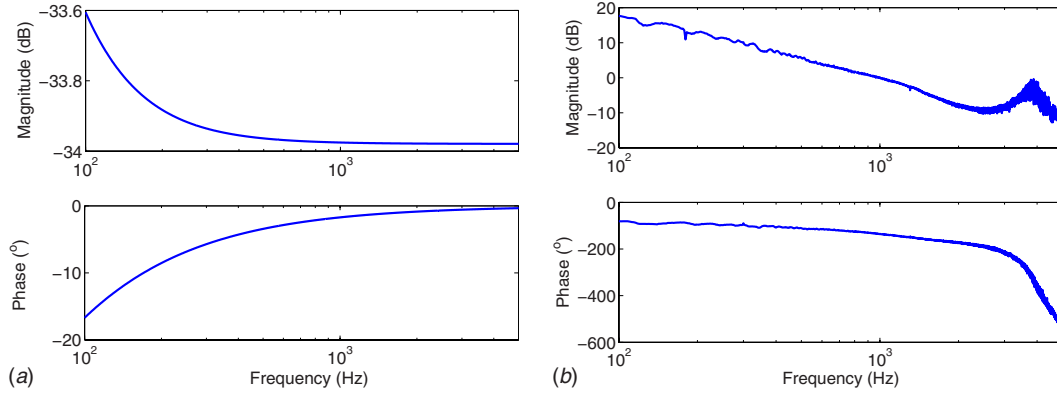


Fig. 7 Frequency response of the PI controller in (a) and the open loop controller-actuator in the near-linear operating regime in (b)

timel tracking control design where an open loop control signal is computed off-line. To improve robustness to operating uncertainties, perturbation feedback using PI control is implemented. The development of the hybrid nonlinear optimal tracking control design follows previous numerical analyses focused on the hysteresis of magnetostrictive actuators for vibration attenuation of beam and plate structures and tracking control of rod structures [24,25,31]. We summarize here key equations associated with nonlinear optimal tracking control and perturbation feedback.

Optimal tracking control employs a cost functional to determine the optimal control input. The cost functional

$$\bar{J} = \frac{1}{2}(\mathbf{C}\mathbf{x}(t_f) - r(t_f))^T P(\mathbf{C}\mathbf{x}(t_f) - r(t_f)) + \int_{t_0}^{t_f} [\mathcal{H} - \lambda^T(t)\dot{\mathbf{x}}(t)]dt \quad (27)$$

penalizes the control input and the error between the Terfenol-D actuator displacement and the prescribed displacement where P penalizes large terminal values on the tracking error, \mathcal{H} is the Hamiltonian, and $\lambda(t)$ is a set of Lagrange multipliers. The Hamiltonian is

$$\mathcal{H} = \frac{1}{2}[(\mathbf{C}\mathbf{x}(t) - r(t))^T Q(\mathbf{C}\mathbf{x}(t) - r(t)) + u^T(t)Ru(t)] + \lambda^T[\mathbf{A}\mathbf{x}(t) + [\mathbf{B}(u)](t) + \mathbf{G}(t)] \quad (28)$$

where penalties on the tracking error and the control input are given by the variables Q and R , respectively.

The minimum of the cost functional in Eq. (27) is determined under the constraint of the differential equation given by Eq. (15).

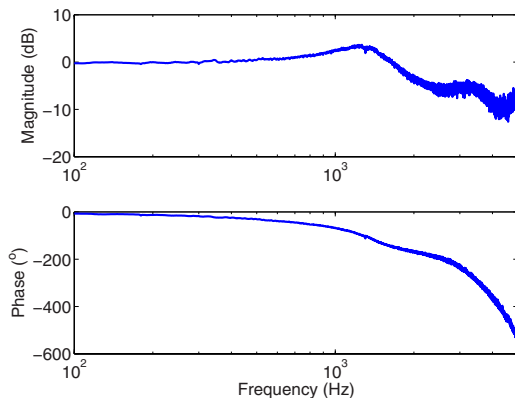


Fig. 8 Frequency response of the closed loop controller-actuator system in the near linear operating regime

By employing Lagrange multipliers, an unconstrained minimization problem is constructed where the stationary condition for the Hamiltonian yields the adjoint relation [32,33]

$$\dot{\lambda}(t) = -\mathbf{A}^T\lambda(t) - \mathbf{C}^T Q \mathbf{C}\mathbf{x}(t) + \mathbf{C}^T Q r(t) \quad (29)$$

and optimal control input

$$u^*(t) = -R^{-1}\left(\frac{\partial \mathbf{B}(u)}{\partial u}\right)^T \lambda(t) \quad (30)$$

The resulting optimality system is

$$\begin{bmatrix} \dot{\mathbf{x}}(t) \\ \dot{\lambda}(t) \end{bmatrix} = \begin{bmatrix} \mathbf{A}\mathbf{x}(t) + [\mathbf{B}(u^*)](t) + \mathbf{G}(t) \\ -\mathbf{A}^T\lambda(t) - \mathbf{C}^T Q \mathbf{C}\mathbf{x}(t) + \mathbf{C}^T Q r(t) \end{bmatrix}$$

$$\mathbf{x}(t_0) = \mathbf{x}_0$$

$$\lambda(t_f) = \mathbf{C}^T P(\mathbf{C}\mathbf{x}(t_f) - r(t_f)) \quad (31)$$

The force due to input fields is included in the input operator $[\mathbf{B}(u^*)](t)$, which directly includes the rate-dependent nonlinear and hysteretic H - M behavior within the control design. This dynamic system results in a two-point boundary value problem, which precludes an efficient Riccati formulation due to the nonlinear nature of the input operator. This system of equations and the boundary conditions are solved using a quasi-Newton method to determine the nonlinear magnetic field input (see Ref. [24] for more details).

An additional step is necessary to implement the control design experimentally using the voltage control amplifier. As discussed in Sec. 3.3, the homogenized energy model can be used to quantify nonlinear inductance. This relation is used to numerically determine the voltage control from Eq. (17) since the current can be determined from the magnetic field in Eq. (30) and the current-field relation in Eq. (18).

The following steps are used to determine the voltage control input: (1) The optimal magnetic field is computed from Eq. (30). (2) The actuator is simulated by applying $u^*(t)$ to Eq. (15) to determine dy/du^* to obtain the nonlinear inductance. (3) The nonlinear voltage control is computed by solving the nonlinear ODE in Eq. (17) numerically. Numerical implementation of Eq. (17) uses a central difference approximation,

$$V_k = \frac{1}{2}(L(M_k) + L(M_{k+1}))\frac{i_{k+1} + i_k}{\Delta t} + \frac{1}{2}R(i_{k+1} + i_k) \quad (32)$$

where a temporal step size Δt is employed, giving a discretization in time defined by $t_k = k\Delta t$. The voltage solved in Eq. (32) is the nonlinear open loop control input used in the experiments.

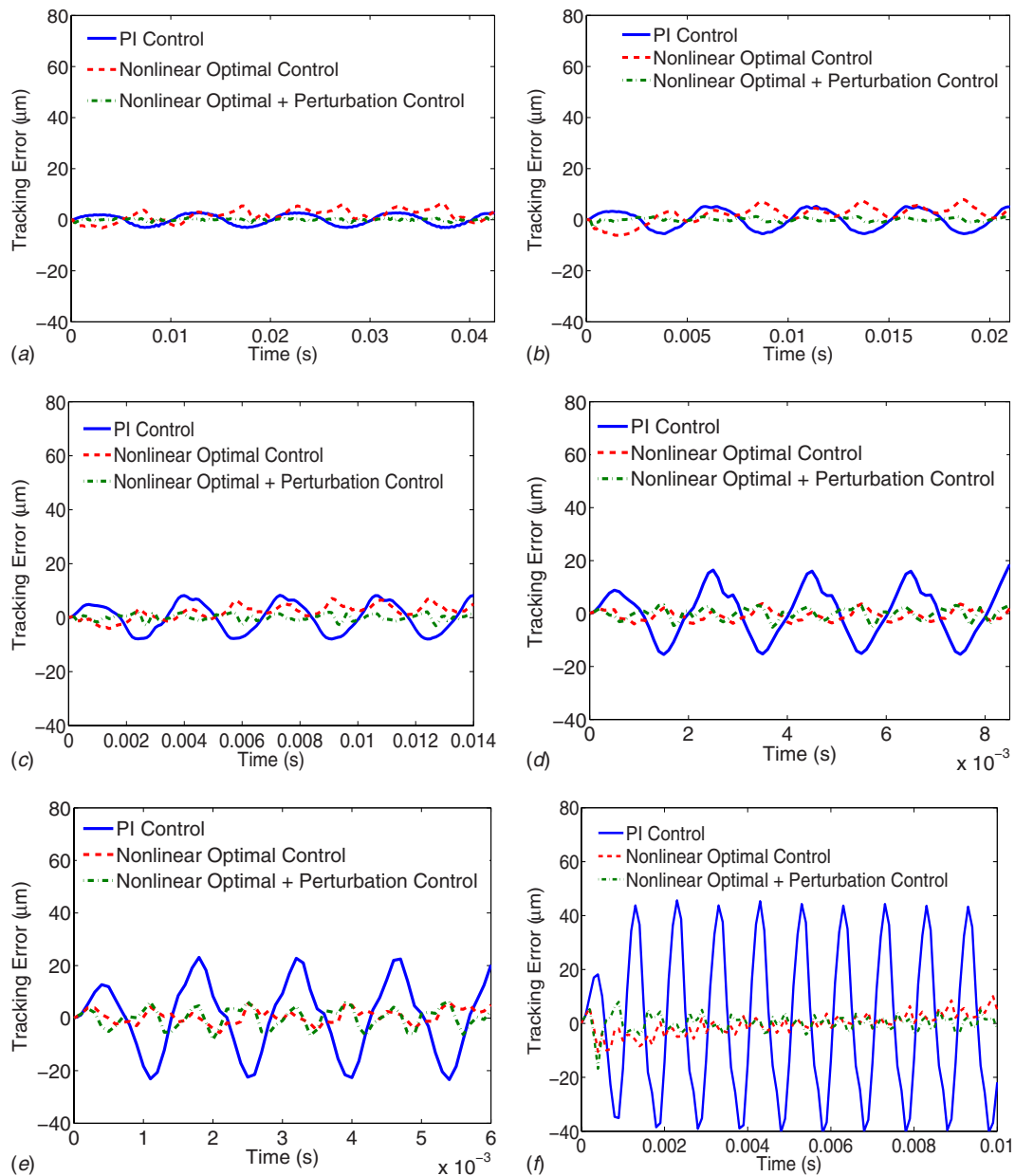


Fig. 9 Comparison of the tracking control performance using PI control, nonlinear open loop optimal control, and nonlinear open loop optimal control with PI perturbation feedback. The frequencies tested range from (a) 100 Hz, (b) 200 Hz, (c) 300 Hz, (d) 500 Hz, (e) 700 Hz, and (f) 1000 Hz. The reference displacement amplitude was 30 μm .

4.2.1 Perturbation Feedback. It is known that open loop controls are not robust with regard to operating uncertainties such as unmodeled constitutive behavior or disturbance loads. To mitigate these effects, PI perturbation feedback about the optimal open loop signal is implemented to improve robustness.

The perturbation control design is identical to the PI controller given in Eq. (26). The perturbation control can be written in the time domain as

$$\delta u(t) = -K_p e(t) - K_I \int_0^t e(s) ds \quad (33)$$

where $e(s)$ is the error between the measured displacement and the reference displacement. The perturbation control input is added to the system given by Eq. (15)

$$\dot{\mathbf{x}}(t) = \mathbf{A}\mathbf{x}(t) + [\mathbf{B}(u^* + \delta u)](t)$$

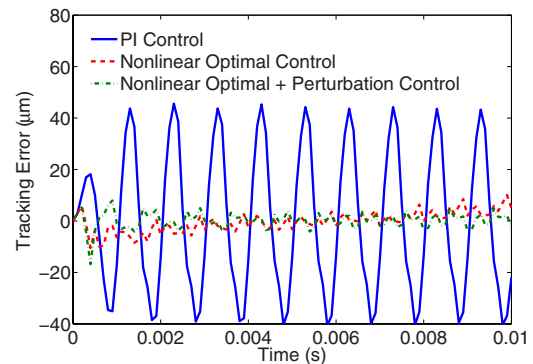


Fig. 10 Tracking control experimental results at 1 kHz expanded from Fig. 9 to illustrate improvements in tracking control between PI control and nonlinear optimal control

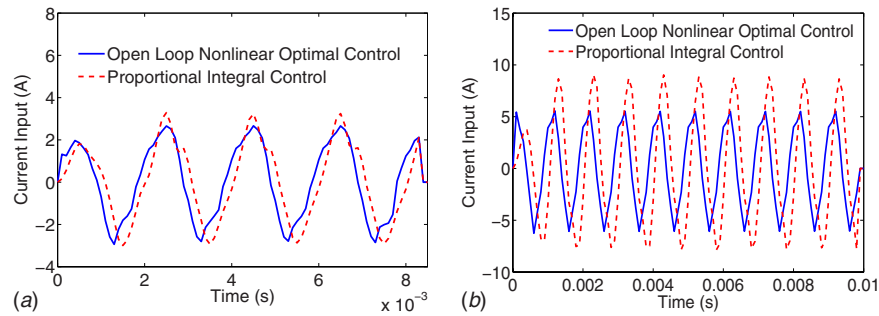


Fig. 11 Comparison of current inputs using open loop nonlinear optimal control and PI control. (a) Current input for the 500 Hz reference displacement. (b) Current input for the 1000 Hz reference displacement.

$$\mathbf{x}(t_0) = \mathbf{x}_0 + \delta \mathbf{x}_0 \quad (34)$$

where the nonlinear input operator includes the optimal open loop control $u^*(t)$ and the perturbation feedback control $\delta u(t)$. Possible variations in the initial conditions are denoted by $\delta \mathbf{x}_0$. The control gains used in the perturbation feedback controller were the same as the PI controller presented in Sec. 4.1.

5 Tracking Control Experimental Results

The performance characteristics of the PI controller, open loop nonlinear optimal control design, and nonlinear optimal controller with PI perturbation feedback is given to illustrate operating regimes where the nonlinear controller is superior. In all the control experiments, a sample frequency of 10 kHz was used. The control experiments were initiated by a half-cycle of 1 Hz sine wave with an amplitude of 1 V. The reference displacement is taken to be zero at the onset of applying control; therefore, the initial remnant displacement occurring after the magnetization half-cycle is subtracted from the total actuator displacement. The commanded reference input to the controller was a sinusoidal signal. The amplitude of the reference signal was chosen to be 30 μm , which represents an operating regime where significant nonlinearities exist, as previously illustrated in Fig. 4. Control experiments for frequencies of 100 Hz, 200 Hz, 300 Hz, 500 Hz, 700 Hz, and 1000 Hz were conducted, and the results are illustrated in Fig. 9 for each control design. The tracking error for each control design is shown to emphasize performance attributes over the frequency range tested. The length of the reference signal in all cases except for the 1 kHz case was 4.25 periods. The 1000 Hz experiment was extended to 10 periods in order to observe the potential effects of drift using the open loop nonlinear optimal controller.

The comparison in tracking performance for each reference displacement signal is illustrated in Fig. 9. Comparable performance was achieved between the PI controller and the nonlinear optimal control design for 100 Hz and 200 Hz reference displacements. Marginal differences in tracking control between PI and the nonlinear control design become apparent at 300 Hz, and at higher frequencies, the tracking error using PI control continues to increase. A phase lag occurs due to the hysteresis as the frequency increases above 500 Hz. As the reference displacement frequency approaches the bandwidth of the PI controller, the amplification in the closed loop system previously shown in Fig. 8 degrades tracking control (see Fig. 9). This is also illustrated in Fig. 10 where the voltage control input is shown for the 500 Hz and 1000 Hz cases. A phase lag is shown between the nonlinear open loop optimal control and the PI controller at 500 Hz, while the PI controller overamplifies the control signal at 1000 Hz. Figure 10 illustrates how the nonlinear open loop control directly compensates for the nonlinear and hysteretic constitutive behavior. It should also be noted that minor errors in drift occur at 1000 Hz using nonlinear open loop control, but this error is corrected by including perturbation feedback, as shown in Fig. 9(f) and expanded in Fig. 11.

The average tracking error for each experiment is quantified using the percent root-mean-square (rms) error and is presented in Table 3. The percent rms error is defined by

$$e_{\text{rms}} = \frac{\frac{1}{T} \int_0^T e^2(t) dt}{\max(y(t)) - \min(y(t))} \quad (35)$$

where T is the final time in each experiment. A direct comparison of percent rms errors between nonlinear control with perturbation and PI control illustrates superior performance at all frequencies tested. The percent error was reduced by more than one order of magnitude at each frequency tested. It should also be noted that open loop nonlinear control and perturbation feedback control gave approximately the same error at frequencies ≥ 500 Hz. This is believed to be related to the bandwidth of the PI controller used for perturbation feedback since the control gains were the same as the PI control design.

6 Discussion and Concluding Remarks

The incorporation of the homogenized energy model in the nonlinear optimal control design was shown to significantly improve tracking control at frequencies up to at least 1000 Hz. Reasonable robustness in model predictions was illustrated by fitting a single set of rate-dependent material parameters to data between 100 Hz and 500 Hz, which was then used in controlling the Terfenol-D actuator up to 1 kHz. As previously noted, only current versus displacement data were measured, which required estimating the current versus magnetization hysteresis loops. Since the induction of the magnetostrictive actuator was not measured, uncertainty in estimating certain rate-dependent model parameters occurred. While this may limit achieving an accurate model for both displacement and magnetization, it illustrates the ability to implement the model-based control design on magnetostrictive actuators in situations where the magnetization is not measurable but only displacement tracking is desired.

Previously, the homogenized energy model has focused on applying a magnetic field to quantify changes in the internal magnetization state. In the present analysis, the homogenized energy

Table 3 Percent rms error for each tracking control experiment illustrated in Fig. 9

Frequency (Hz)	PI control	Open loop optimal control	Perturbation control
100	0.7%	1.4%	0.02%
200	2.3%	2.2%	0.08%
300	4.8%	1.7%	0.2%
500	15%	0.73%	0.8%
700	29%	1.2%	2.4%
1000	94%	2.2%	1.3%

model was used to relate magnetic fields to voltage inputs. A simple relation was presented to relate the magnetic field in the Terfenol-D rod to the current in the wound wire solenoid. This approach assumed full penetration of the magnetic field for the frequency range considered, which neglects eddy currents. The Terfenol-D rod was not laminated; therefore, the possibility of generating eddy currents is likely to occur in the frequency range tested. Further work is required to quantify this behavior and identify the appropriate method for including eddy currents in the model-based control design. The effect of ferromagnetic switching behavior on the nonlinear inductance was included in the model, as previously illustrated in Fig. 5. The incorporation of nonlinear induction in regions where more ferromagnetic switching is expected to occur reduced modeling errors of current-voltage behavior, as shown in Fig. 5, but approximating the inductance as linear may be sufficient depending on the performance requirements needed and the magnitude of ferromagnetic switching.

The nonlinear optimal control design has focused on applications where the reference displacement is known in advance and precise control is desired at relatively high speed. For such applications, which may include high speed machining or micro- to nanopositioning systems, the nonlinear control input can be computed off-line and then implemented in real-time control applications. Although the numerical procedure requires convergence of a nonlinear two-point boundary value problem, once the numerical procedure is developed, the control input for most reference signals (within physical limitations) can be quantified. This approach provides an alternative to nonlinear inverse compensator designs, which depend on the ability to invert the constitutive model efficiently in real time. It should also be noted that smooth reference displacement signals were considered here. In cases where the reference signal is nonsmooth, higher order harmonics may be induced and may require extending the model to include higher order dynamic behavior and coupling to ferromagnetic switching. This may also have implications on the perturbation feedback design since PI control may not provide sufficient control of the closed loop system.

The PI controller provided good tracking control at 100 Hz and 200 Hz, and performance degradation began to occur at 300 Hz. Amplification in the closed loop response (see Fig. 8) increased the tracking error as the frequency approached the bandwidth of the system (see Figs. 9(a)–9(f)). In addition, the effects of nonlinearities and hysteresis previously illustrated in Fig. 4(d) become significant at higher frequencies, which limits precise displacement control. Conversely, when the nonlinear optimal control design is implemented with perturbation feedback, the tracking errors are reduced and good performance is achieved up to 1000 Hz. These experimental results used perturbation control gains that were identical to the PI control gains. Although larger gains were considered for perturbation control, reduction in tracking error was not achieved. Whereas the inclusion of open loop nonlinear control is expected to reduce the effect of phase lag from nonlinearities and hysteresis and to allow the application of larger perturbation control gains, this was not the case. More work is required to identify this issue. Despite this effect, the hybrid nonlinear control design provides considerable improvements in bandwidth by including the homogenized energy model in the control design. Additionally, due to the general ferroic homogenized energy modeling framework, the control design can be potentially applied to a number of smart material systems and structures that use ferroelectric, magnetostrictive, or shape memory alloys.

Acknowledgment

The authors gratefully acknowledge support from the Air Force Office of Scientific Research through Grant No. AFOSR-FA9550-04-1-0203. The authors also wish to acknowledge Dr. Julie

Slaughter of Etrema Products, Inc., for supplying the Terfenol-D material used in this study.

References

- [1] Park, S.-E., and Shout, T., 1997, "Ultrahigh Strain and Piezoelectric Behavior in Relaxor Based Ferroelectric Single Crystals," *J. Appl. Phys.*, **82**(4), pp. 1804–1811.
- [2] Giessibl, F., 2003, "Advances in Atomic Force Microscopy," *Rev. Mod. Phys.*, **75**, pp. 949–983.
- [3] Nealis, J., and Smith, R., 2007, "Model-Based Robust Control Design for Magnetostrictive Transducers Operating in Hysteretic and Nonlinear Regimes," *IEEE Trans. Control Syst. Technol.*, **15**(1), pp. 22–39.
- [4] Lynch, C., 1996, "The Effect of Uniaxial Stress on the Electro-Mechanical Response of 8/65/35 PLZT," *Acta Mater.*, **44**(10), pp. 4137–4148.
- [5] O'Handley, R., Murray, S., Marioni, M., Nembach, H., and Allen, S., 2000, "Phenomenology and Giant Magnetic-Field-Induced Strain in Ferromagnetic Shape-Memory Materials," *J. Appl. Phys.*, **87**(9), pp. 4712–4717.
- [6] Smith, R., Salapaka, M., Hatch, A., Smith, J., and De, T., 2002, "Model Development and Inverse Compensator Design for High Speed Nanopositioning," *Proceedings of the 41st IEEE Conference on Decision Control*, pp. 3652–3657.
- [7] Cavallo, A., Natale, C., Pirozzi, S., Visone, C., and Formisano, A., 2004, "Feedback Control Systems for Micropositioning Tasks With Hysteresis Compensation," *IEEE Trans. Magn.*, **40**(2), pp. 876–879.
- [8] Tan, X., and Baras, J., 2004, "Modeling and Control of Hysteresis in Magnetostrictive Actuators," *Automatica*, **40**, pp. 1469–1480.
- [9] Ge, P., and Jouaneh, M., 1996, "Tracking Control of a Piezoceramic Actuator," *IEEE Trans. Control Syst. Technol.*, **4**(3), pp. 209–216.
- [10] Janocha, H., and Kuhnen, K., 2000, "Real-Time Compensation of Hysteresis and Creep in Piezoelectric Actuators," *Sens. Actuators, A*, **79**, pp. 83–89.
- [11] Majima, S., Kodama, K., and Hasegawa, T., 2001, "Modeling of Shape Memory Alloy Actuator and Tracking Control System With the Model," *IEEE Trans. Control Syst. Technol.*, **9**(1), pp. 54–59.
- [12] Brown, W., 1966, *Magnetoelastic Interactions*, Springer-Verlag, Berlin.
- [13] Jiles, D., 1991, *Introduction to Magnetism and Magnetic Materials*, Chapman and Hall, New York.
- [14] Aharoni, A., 1996, *Introduction to the Theory of Ferromagnetism*, Oxford Science, New York.
- [15] Armstrong, W., 2002, "A Directional Magnetization Potential Based Model of Magnetoelastic Hysteresis," *J. Appl. Phys.*, **91**(4), pp. 2202–2210.
- [16] Bertotti, G., 1998, *Hysteresis in Magnetism: For Physicists, Materials Scientists, and Engineers*, Academic, San Diego, CA.
- [17] Galinaitis, W., and Rogers, R., 1997, "Compensation for Hysteresis Using Bivariate Preisach Models," *Proceedings of SPIE, Smart Structure and Materials 1997: Mathematics and Control in Smart Structures*, San Diego, CA.
- [18] Smith, R., Seelecke, S., Dapino, M., and Ounaies, Z., 2006, "A Unified Framework for Modeling Hysteresis in Ferroic Materials," *J. Mech. Phys. Solids*, **54**(1), pp. 46–85.
- [19] Smith, R., Dapino, M., and Seelecke, S., 2003, "A Free Energy Model for Hysteresis in Magnetostrictive Transducers," *J. Appl. Phys.*, **93**(1), pp. 458–466.
- [20] Smith, R., Seelecke, S., Ounaies, Z., and Smith, J., 2003, "A Free Energy Model for Hysteresis in Ferroelectric Materials," *J. Intell. Mater. Syst. Struct.*, **14**(11), pp. 719–739.
- [21] Smith, R., Hatch, A., Mukherjee, B., and Liu, S., 2005, "A Homogenized Energy Model for Hysteresis in Ferroelectric Materials: General Density Formulations," *J. Intell. Mater. Syst. Struct.*, **16**(9), pp. 713–732.
- [22] Smith, R., 2005, *Smart Material Systems: Model Development*, SIAM, Philadelphia, PA.
- [23] Smith, R., Dapino, M., Braun, T., and Mortensen, A., 2006, "A Homogenized Energy Framework for Ferromagnetic Hysteresis," *IEEE Trans. Magn.*, **42**(7), pp. 1747–1769.
- [24] Smith, R., 1995, "A Nonlinear Optimal Control Method for Magnetostrictive Actuators," *J. Intell. Mater. Syst. Struct.*, **6**(6), pp. 468–486.
- [25] Oates, W., and Smith, R., 2008, "Nonlinear Optimal Control Techniques for Vibration Attenuation Using Nonlinear Magnetostrictive Actuators," *J. Intell. Mater. Syst. Struct.*, **19**(2), pp. 193–209.
- [26] Braun, T., Smith, R., and Dapino, M., 2006, "Experimental Validation of a Homogenized Energy Model for Magnetic After-Effects," *Appl. Phys. Lett.*, **88**, pp. 122511–122513.
- [27] Smith, R., and Dapino, M., 2006, "A Homogenized Energy Model for the Direct Magnetomechanical Effect," *IEEE Trans. Magn.*, **42**(8), pp. 1944–1957.
- [28] Dapino, M., Smith, R., and Flatau, A., 2000, "A Structural Strain Model for Magnetostrictive Transducers," *IEEE Trans. Magn.*, **36**(3), pp. 545–556.
- [29] Oates, W., and Smith, R., 2008, "Nonlinear Optimal Control Techniques for Vibration Attenuation Using Nonlinear Magnetostrictive Actuators," *J. Intell. Mater. Syst. Struct.*, **19**(2), pp. 193–209.
- [30] Serway, R., 1990, *Physics for Scientists and Engineers*, Saunders, Philadelphia.
- [31] Oates, W., and Smith, R., 2007, "Nonlinear Perturbation Control for Magnetic Transducers," *IEEE Conference on Decision and Control*.
- [32] Bryson, A., and Ho, Y.-C., 1969, *Applied Optimal Control*, Blaisdell, Waltham, MA.
- [33] Lewis, F., and Syrmos, V., 1995, *Optimal Control*, Wiley, New York.